Chapter 6

Electronic Band Structures and Phase Transitions of Ferroelectric and Multiferroic Oxides

Zhigao Hu, Junhao Chu, Yawei Li, Kai Jiang and Ziqiang Zhu

Additional information is available at the end of the chapter

http://dx.doi.org/10.5772/52189

1. Introduction

Perovskite ferroelectric (FE) materials have attracted considerable attention for a wide range of applications, such as dynamic random access memories (DRAM), microwave tunable phase shifters and second harmonic generators (SHGs). [1–3] Moreover, materials that have coupled electric, magnetic, and structural order parameters that result in simultaneous ferroelectricity, ferromagnetism, and ferroelasticity are known as multiferroics. [4–6] These multiferroics materials have attracted a lot of attention in recent years because they can potentially offer a whole range of new applications, including nonvolatile ferroelectric memories, novel multiple state memories, and devices based on magnetoeletric effects. Although there are some reports on the electrical and magnetic properties of perovskite-type ferroelectric and multiferroics materials, optical properties and electronic transitions have not been well investigated up to now. On the other hand, phase transition is one of the important characteristics for the ferroelectric/multiferroics system. As we know, the phase transition is strongly related to the structural variation, which certainly can result in the electronic band modifications. Therefore, one can study the phase transition of the above material systems by the corresponding spectral response behavior at different temperatures.

Among these materials, barium strontium titanate (BST) has been considered to be one of the most promising candidates for devices due to its excellent dielectric properties of high dielectric functions, low leakage current and an adjustable Curie temperature T_c through variation of the composition between barium titanate (BT) and strontium titanate (ST). However, the limited figure of merit at high frequency microwave region restricts the BST practical applications. In order to improve the physical properties of the BST materials, introducing small compositions of dopants has been used for several decades. Many experimental and theoretical studies have been performed on the dielectric properties of BST in the ferroelectric state by adding dopants such as Magnesium [7, 8], Aluminum [9], Manganese (Mn) [10–12], Samarium [13], and different rare earth [14], In particular, the Mn

doping BST shows some advantages in reducing the dielectric loss, enhancing the resistivity, and increasing dielectric tunability. It can significantly improve the dielectric properties, which makes it a potential candidate for microwave elements. For example, the Mn doping can cause the variation of the oxygen vacancy, which is the crucial role in modifying the dielectric loss mechanism. On the other hand, the doping of Mn can also reduce the dielectric constant peak and broaden the dielectric phase transition temperature range, which results in a smaller temperature coefficient of capacitance in BSMT materials. [10] Therefore, it is important to further investigate the physical properties of BSMT materials in order to develop the potential applications.

Meanwhile, many research groups have focused on the doping effect on the fabrications and dielectric properties for strontium barium niobate $SrBi_2Nb_2O_9$ (SBN) materials. [15–20] The substitution of Ca ions in the Sr site for the SBN ceramic induced the T_C increasing, which is useful for the application in high-temperature resonators. [15, 18] However, the substitution of some rare earth ions such as La^{3+} or Pr^{3+} for Bi^{3+} in the Bi_2O_2 layers can result in a shift for the T_C to lower temperature. [16, 20, 21] It is found that the behavior of the Nd-doped SBN ceramic tends to change from a normal ferroelectrics to a relaxor type ferroelectrics owing to the introduction of Nd ions in the Bi_2O_2 layers. [16, 17, 20, 22] Up to now, a detailed understanding of the lattice dynamic properties and the phase transition behavior of Nd-doped SBN ceramics are still lacking. Raman spectroscopy is a sensitive technique for investigating the structure modifications and lattice vibration modes, which can give the information on the changes of lattice vibrations and the occupying positions of doping ions. Thus, it is a powerful tool for the detection of phase transition in the doping-related ferroelectric materials. [22, 23]

The optical properties such as the dielectric functions provide an important insight on dielectric and ferroelectric behaviors of the material and play an important role in design, optimization, and evaluation of optoelectronic devices. [24–27] In addition, the doping of Mn or Nd can induce more defects in the lattice structure, which can affect its electronic band structures and optoelectronic properties. Hence, the doping composition dependence of optical properties for BST and SBN ceramics is technically important for practical optoelectronic device development. Compared to film structure, the optical properties of bulk material (single crystals and dense ceramics) are not affected by interface layer, stress from clamping by the substrate, non-stoichiometry and lattice mismatch between film and substrate. Hence, it is desirable to carry out a delicate investigation regarding the optical properties of the BSMT and SBNN ceramics. Note that spectroscopic ellipsometry (SE), Raman scattering, and transmittance spectra are potentially valuable techniques for the studies of ferroelectric materials due to their high sensitivity of local structure and symmetry. Compared with the other techniques, they can provide dielectric functions of the materials. SE and transmittance spectra can provide optical band gap and optical conductivity, whereas Raman spectra can provide Raman-active modes of the materials. [28–31]

On the other hand, bismuth ferrite ($BiFeO_3$, BFO) is known to be the only perovskite material that exhibits multiferroic at room temperature (RT). At RT, it is a rhombohedrally distorted ferroelectric perovskite with the space group *R3c* and a Curie temperature (T_C) of about 1100 K. [32–36] Since the physical properties of BFO films are related to their domain structure and phase states, which is sensitive to the applied stress, composition, and fabrication condition for BFO materials. PLD technique has the ability to exceed the solubility of magnetic impurity and to permit high quality film grown at low substrate temperature. Recent studies of photoconductivity, [35] photovoltaic effect, [37] and low open circuit voltage in a working solar device, [38] illustrate the potential of polar oxides as the active photovoltaic material.

http://dx.doi.org/10.5772/52189

In spite of the promising properties, there are no systematical reports focused on the optical properties of BFO films. In order to make BFO useful in actual electrical and optoelectronic devices, the physical properties, especially for electronic band structure and optical response behavior, need to be further clarified.

The objectives of the chapter will tentatively answer the interesting questions: (1) Is there an effective method to directly analyze electronic structure of FE materials by optical spectroscopy? (2) What kind of temperature dependence have FE oxides from band-to-band transitions? (3) Can spectral response at high-temperature be used to judge phase transition? Correspondingly, this chapter is arranged in the following way. In Sec. 2, detailed growths of $Ba_{0.4}Sr_{0.6-x}Mn_xTiO_3$ (BSMT), $SrBi_{2-x}Nd_xNb_2O_9$ (SBNN) ceramics and BFO films are described; In Sec. 3, solid state spectroscopic techniques are introduced; In Sec. 4, electronic band structures of BSMT ceramics are presented; In Sec. 5, phase transitions of SBNN ceramics are derived; In Sec. 6, temperature effects on electronic transitions of BFO films have been discussed; In Sec. 7, the main results and remarks are summarized.

2. Experimental

2.1. Fabrications of FE ceramics

The ceramics based on $Ba_{0.4}Sr_{0.6-x}Mn_xTiO_3$ (with x = 1, 2, 5 and 10%) specimens were prepared by the conventional solid-state reaction sintering. High purity $BaCO_3$ (99.8%), $SrCO_3$ (99.0%), TiO_2 (99.9%), and $MnCO_3$ were used as the starting materials. Weighted powers were mixed by ball milling with zirconia media in the ethanol as a solvent for 24 h and then dried at 110 °C for 12 h. After drying, the powders were calcined at 1200 °C for 4 h, and then remilled for 24 h to reduce the particle size for sintering. The calcined powders were added with 8 wt.% polyvinyl alcohol (PVA) as a binder. The granulated powders were pressed into discs in diameter of 10 mm and thickness of 1.0 mm. The green pellets were kept at 550 °C for 6 h to remove the solvent and binder, followed by sintering at 1400 °C for 4 h. More details of the preparation process can be found in Ref. [39]. On the other hand, the SBNN (x=0, 0.05, 0.1, and 0.2) ceramics were prepared by a similar method, and $SrCO_3$, Bi_2O_3, Nb_2O_5, and Nd_2O_3 were used as the starting materials. Details of the fabrication process for the ceramics can be found elsewhere. [17, 40]

2.2. Depositions of BFO films

The $BiFeO_3$ films were deposited on c-sapphire substrates by the PLD technique. The $BiFeO_3$ targets with a diameter of 3 cm were prepared through a conventional solid state reaction method using reagent-grade Bi_2O_3 (99.9%) and Fe_2O_3 (99.9%) powders. Weighed powders were mixed for 24 h by ball milling with zirconia media in ethanol and then dried at 100 °C for 12 h. The dried powders were calcined at about 680 °C in air for 6 h to form the desired phase, and followed by sintering at about 830 °C for 2 h. Before the deposition of the BFO films, c-sapphire substrates need to be cleaned in pure ethanol with an ultrasonic bath to remove physisorbed organic molecules from the surfaces, followed by rinsing several times with de-ionized water. Then the substrates were dried in a pure nitrogen stream before the film deposition. A pulsed Nd:YAG (yttrium aluminum garnet) laser (532 nm wavelength, 5 ns duration) operated with an energy of 60 mJ/pulse and repetition rate of 10 Hz was used as the ablation source. The films were deposited immediately after the target was

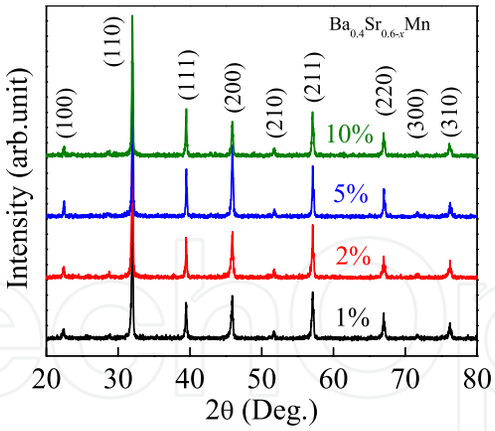

Figure 1. The XRD patterns of the BSMT ceramics with the Mn composition of 1, 2, 5 and 10%, respectively.

preablated in order to remove any surface contaminants. The distance between the target and the substrate was kept at 3 cm. The deposition time was set to about 30 min. Finally, the films were annealed at 600 °C in air atmosphere by a rapid thermal annealing process. A detailed preparation of the films can be found in Ref. [6].

3. Optical spectroscopy

The ellipsometric measurements were carried out in the photon energy range of 0.7-4.2 eV (300-1700 nm) with a spectral resolution of 5 nm by near-infrared-ultraviolet (NIR-UV) SE (SC630UVN by Shanghai Sanco Instrument, Co., Ltd.). The measurements were performed under the incident angle of 67° for all the ceramics corresponding to the experimental optimization near the Brewster angle of the BSMT. Raman scattering experiments were carried out using a Jobin-Yvon LabRAM HR 800 UV micro-Raman spectrometer, excited by a 632.8 nm He-Ne laser with a spectral resolution of 0.5 cm^{-1}. Temperature dependent measurements from 80 to 873 K were performed using the Linkam THMSE 600 heating stage, and the set-point stability is of better than 0.5 K. The normal-incident transmittance spectra were recorded using a double beam ultraviolet-infrared spectrophotometer (PerkinElmer Lambda 950) at the photon energy from 0.5 to 6.5 eV (190-2650 nm) with a spectral resolution of 2 nm. The samples at 5.3-300 K were mounted into an optical cryostat (Janis SHI-4-1) for variable temperature experiments. [41]

4. Electronic band structures of BSMT ceramics

The XRD patterns of the BSMT ceramics with different Mn composition are shown in Fig. 1 and no secondary phase appears within the detection limit of the XRD. Besides the strongest (110) peak, some weaker peaks (100), (111), (200), (210), (211), (220) can be also observed, which indicate that the ceramics are polycrystalline with single perovskite phase. The diffraction patterns are fitted by the Gaussian lineshape analysis to extract the peak positions and full width at half maximum (FWHM). The lattice constant a of the BSMT ceramics, which can be estimated from the (110) diffraction peak, is calculated to be about 3.954 Å. [39] The ionic radius of Mn^{2+} (1.27 Å) is smaller than that of Sr^{2+} (1.44 Å) and Ba^{2+} (1.61 Å), and is larger than that of Ti^{4+} (0.61 Å), which can be attributed to the change of the lattice constant. When the Mn composition is below 5%, the (110) diffraction peak positions shift from smaller angles to larger angles and the lattice constant slightly decreases, which can be

http://dx.doi.org/10.5772/52189

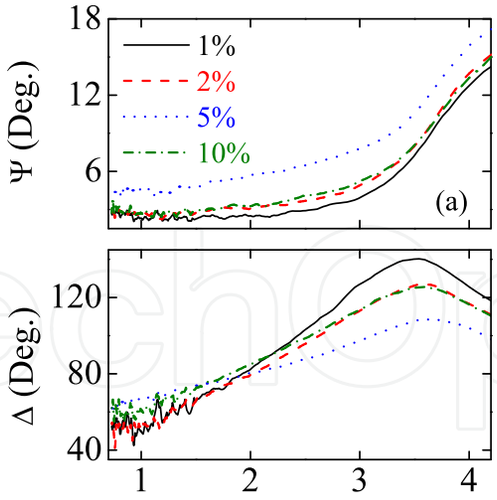

Figure 2. Experimental ellipsometric data (a) Ψ and (b) Δ for the BSMT ceramics from near-infrared to ultraviolet photon energy region at the incident angle of 67°. (Figure reproduced with permission from [39]. Copyright 2012, Springer.)

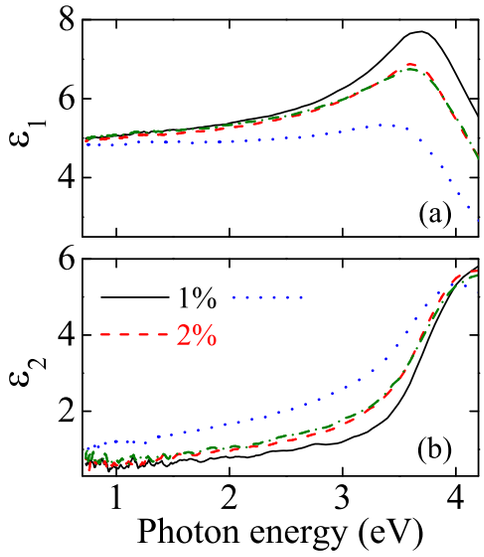

Figure 3. The (a) real and (b) imaginary parts of the NIR-UV dielectric functions for the BSMT ceramics with different Mn composition. (Figure reproduced with permission from [39]. Copyright 2012, Springer.)

ascribed to the fact that Mn occupies the A site together with Ba^{2+} and Sr^{2+}. In order to reduce distortion of the crystal lattice, the Mn mainly substitutes Sr^{2+} because the differences in ionic radius between Mn ion and Ba ion is larger than that between Mn and Sr. On the other hand, when the Mn composition is larger than 5%, the excess Mn can also substitute the Ti site, which results in the increase of the lattice constant and the smaller shift of the peak position. It can be concluded that the Mn ions substitute Sr sites of the BST lattice at first, then occupy Ti sites when the Mn composition is beyond 5%.

The experimental ellipsometric spectra of Ψ and Δ recorded at an incident angle of 67° for the BSMT ceramics are depicted in Figs. 2(a) and (b), respectively. The observed changes in the Ψ and Δ data for different Mn composition may be attributed to the lattice distortion and variation in atomic coordinate. Because the sample is bulk material with a thickness of several millimeters, the dielectric functions of the BSMT ceramics can be directly calculated

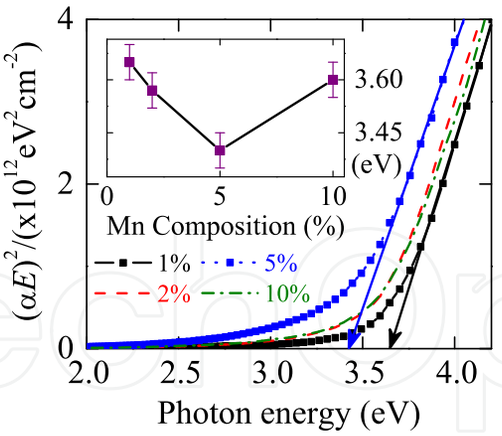

Figure 4. Absorption coefficient *vs*. incident photon energy near the optical band gap of the BSMT ceramics. The insert is the optical band gap E_g with the different Mn composition. (Figure reproduced with permission from [39]. Copyright 2012, Springer.)

according to the ellipsometric spectra Ḟigs. 3(a) and (b) show the real (ε_1) and imaginary (ε_2) parts of the dielectric functions in the photon energy range of 0.7-4.2 eV, respectively. The evolution of ε with the photon energy is a typical optical response behavior of ferroelectric and/or semiconductors. The optical band gap (E_g) of the BSMT ceramics is one of the important optical behaviors, which is calculated by considering a direct transition from the VB to the CB when the photon energy falls on the materials. In the BSMT system, the VB is mainly composed of the O 2*p* orbital and the CB is mainly composed of the Ti 3*d* orbital. It should be noted that because of the splitting of the Ti 3*d* conduction bands into t_{2g} and e_g subbands, the lowest CB arises from the threefold degenerate Ti 3*d* t_{2g} orbital, which has lower energy than the twofold degenerate Ti 3*d* e_g orbital. [42] The absorption coefficient related E_g of the BSMT ceramics can be determined according to the Tauc's law: $(\alpha E)^2 = A(E - E_g)$, where A is a constant, α and E are the absorption coefficient and incident photon energy, respectively. For the allowed direct transition, the straight line between $(\alpha E)^2$ and E will provide the value of the band gap, which is extrapolated by the linear portion of the plot to $(\alpha E)^2$=0, as seen in Fig. 4. The E_g is estimated to 3.65, 3.57, 3.40 and 3.60 eV corresponding to x=1, 2, 5 and 10% for the BSMT ceramics, respectively, as shown in the inset of Fig. 4. The results suggest that the band gap of the BSMT ceramics decreases and then increases with increasing Mn composition.

As we know, the optical band gap can be affected by some factors such as grain size, oxygen vacancy, stress and amorphous nature of the materials. [2] The decreasing trend of the band gap with the Mn composition below 5% can be attributed to the increase of the grain size and the smaller lattice constant, which are caused by the Mn introduction in the A sites. When the Mn composition is 10%, there is a sharp increase in the optical band gap because the excess Mn will substitute the Ti site at the Mn composition of 10%, causing the increase of the oxygen vacancies. In addition, the creation of an oxygen vacancy which is associated with the generation of free charge carriers can be described as the following: $MnO(-TiO_2) \rightarrow Mn''_{Ti} + V^{\cdot\cdot}_O + O_O$; $O_O \rightarrow V^{\cdot\cdot}_O + 2e^- + 1/2O_2$, where $V^{\cdot\cdot}_O$ represents the doubly charged oxygen vacancy, O_O is an oxygen ion at its normal site, e^- is the free electronic charge generated through the vacancy formation. [9, 43] The heavy doping blocks the lowest states in the CB and the effective band-gap increases, which is known as the Burstein-Moss (BM) effect. [44] When a large number of vacancy-related charge carriers are

http://dx.doi.org/10.5772/52189

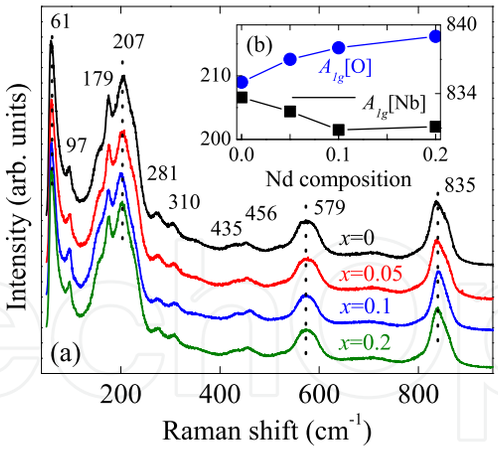

Figure 5. Raman scattering spectra of the SBNN ceramics with different Nd composition (x) recorded at RT. The dashed lines clearly indicate some Raman-active phonon modes. The inset shows the peak frequency variation of the A_{1g}[Nb] phonon mode at about 207 cm^{-1} and the A_{1g}[O] phonon mode at about 836 cm^{-1} as a function of Nd composition. (Figure reproduced with permission from [46]. Copyright 2012, Wiley.)

generated in the system, the lowest lying states in the CB are filled and the vertical distance needed for the optical transition increases. [44] Hence, it can be concluded that, when the Mn composition is 10%, the sharply increase in the band gap may be attributed to the BM shift caused by electrons generated by oxygen vacancies. Besides, the grain size for the ceramic decreases induced by the heavy doping with the Mn composition of 10%, which may also result in a sharply increase of the optical band gap. It can be concluded that the difference of the optical band gap could be due to the dopant composition, the oxygen vacancies, and the crystallinity of the BSMT ceramics.

5. Phase transitions of SBNN ceramics

The general formula of bismuth layer structure ferroelectrics (BLSFs) is given as $(Bi_2O_2)^{2+}(A_{m-1}B_mO_{3m+1})^{2-}$, where A and B are the two types of cations that enter the perovskite unit, and m is the the number of perovskite unit cell between bismuth oxide layers. [20] SBN, which is known to be m=2 member of BLSFs family, has been regarded as a promising ferroelectric material due to low dielectric constants and excellent fatigue resistance. [40] Fig. 5(a) shows the Raman spectra of the SBNN ceramics with different Nd compositions at RT in the spectral range of $50-950$ cm^{-1}. The Raman selection rules allow 18 phonon modes ($4A_{1g}+2B_{1g}+6B_{2g}+6B_{3g}$) for SBN ceramics at RT. [45] However, less than 10 phonon modes are observed because of the possible overlap of the same symmetry vibration or the weak feature of some vibration bands. [46, 47] According to the assignment of $SrBi_2Nb_2O_9$ single crystal, [45] the Raman phonon modes at about 61, 207 and 835 cm^{-1} can be assigned to the A_{1g} phonon mode, the vibrations at about 179 and 579 cm^{-1} can be assigned to the E_g phonon mode. However, the assignment of other phonon modes are still not clear now. The internal vibrations of NbO_6 octahedra occur in the high-frequency mode region above 200 cm^{-1} because the intragroup binding energy within the NbO_6 octahedra is much larger than the intergroup or crystal binding energy. [15] The composition dependence of the frequencies for two typical phonon modes is illustrated in Fig. 5(b). Note that the A_{1g}[Nb] phonon mode at 207 cm^{-1}, which arises from the distortion of NbO_6 octahedra, generally decreases with the Nd composition, whereas the A_{1g}[O] phonon mode at 835 cm^{-1} mode corresponding to the symmetric Nb−O stretching vibration, increases with the introduction of Nd ions.

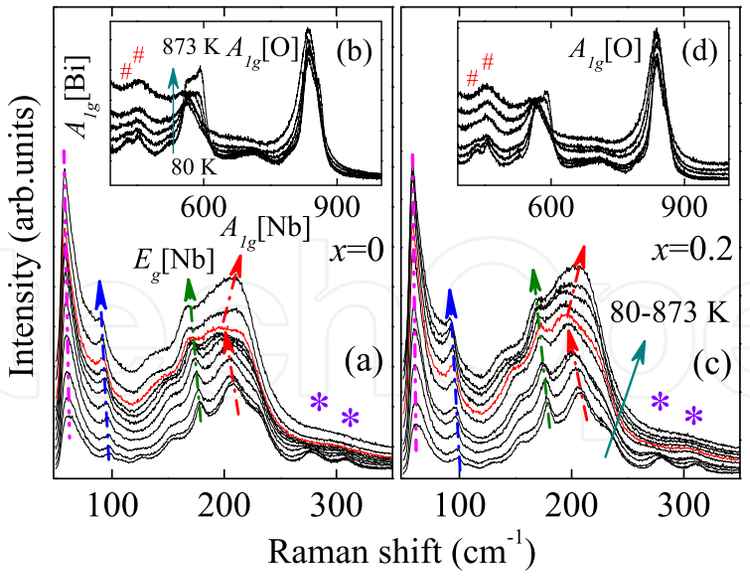

Figure 6. Temperature dependence of the SBNN ceramics with the composition of (a)(b) x=0 and (c)(d) x=0.2. The solid arrows indicate the temperature increasing from 80 K to 873 K, and the dash arrows show the shift of the frequency for the phonon modes with the temperature. The symbol asterisk (∗) and pound sign (#) indicate the two weak E_g phonon modes in the range of 281-310 cm^{-1} and 435-456 cm^{-1}, respectively. (Figure reproduced with permission from [46]. Copyright 2012, Wiley.)

In order to further understand the effect of Nd^{3+} ion substitution on the phonon modes, Fig. 6 presents the temperature dependence of the Raman spectra for the SBNN ceramics with two Nd compositions of x=0 and 0.2 in the temperature range from 80 to 873 K. It suggests that the intensities for all the phonon modes increase with the temperature except for the phonon mode at about 579 cm^{-1}, whose peak has been overwhelmed at high temperature. The broadening band can be assigned to a rigid sublattice mode, in which all the positive and negative ion displacements are equal and opposite. [48] It is found that a strong broadening peak can be observed at 80 K due to the combined effects of two modes splitting from the E_g character mode. However, with increasing the temperature, the frequency and intensity of the mode present a decreasing trend. Because the mode is assigned to the asymmetric Nb−O vibration, it can be concluded that the NbO_6 octahedra is sensitive to the temperature. On the other band, the phonon modes at about 281 and 310 cm^{-1} (labeled by ∗), which are associated with the O−Nb−O bending, become more difficult to be distinguished as the temperature increases and disappear at high temperature. Similar phenomena can be observed for the phonon modes in the range of 435-456 cm^{-1} (labeled by #). The band at about 456 cm^{-1}, which is described to a Ti−O torsional mode, has been assigned as the E_g character and splits into two phonon modes centered at 435 and 456 cm^{-1} at lower temperature. As pointed out by Graves *et al*., [45] it can be ascribed to the fact that the several E_g phonon modes split into the B_{2g} and B_{3g} phonon modes during the tetragonal to orthorhombic transition. Moreover, the splitting of the phonon modes reveals the structural changes in the SBNN ceramics with the temperature.

Considering that the phase transition temperature is related to the distortion extent of the NbO_6 octahedra for the SBNN ceramics, the temperature dependence of the Raman shift for the A_{1g}[Nb] phonon mode is plotted in Fig. 7(a)-(d). For all the SBNN ceramics, the decrease of the A_{1g}[Nb] phonon mode can be observed as the temperature is increased. Note that an obviously anomalous vibration occurs around the phase transition temperatures: the Raman shift sharply increases with increasing the temperature. In addition, the temperature

http://dx.doi.org/10.5772/52189

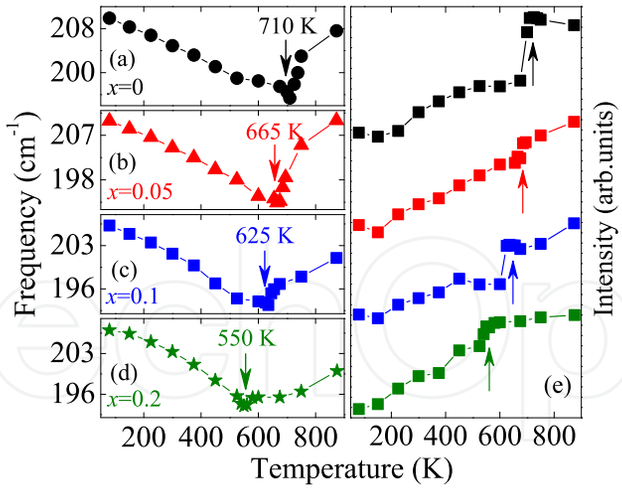

Figure 7. (a)-(d) Raman shift and (e) intensities of the A_{1g}[Nb] phonon mode as a function of the temperature for the SBNN ceramics. The arrows indicate that the anomalous vibration occurs around the ferroelectric to paraelectric phase transition temperatures. (Figure reproduced with permission from [46]. Copyright 2012, Wiley.)

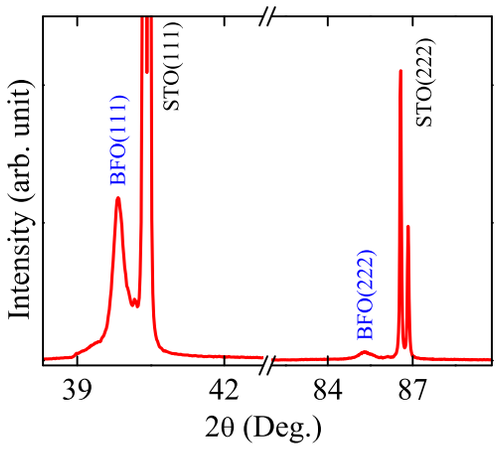

Figure 8. The XRD patterns of the BFO films deposited on STO (111) substrate. (Figure reproduced with permission from [5]. Copyright 2010, American Institute of Physics.)

of the anomalous points is different for the four ceramics: 710 K for x=0, 665 K for x=0.05, 625 K for x=0.1 and 550 K for x=0.2. The different anomalous points can be ascribed to the Nd^{3+} incorporation in the Bi_2O_2 layers. In addition, the phase transition from the orthorhombic to the tetragonal phase may occur at the temperature when the frequency of the A_{1g}[Nb] phonon mode shows the anomalous behavior. Therefore, the sharp change in the temperature dependence of both wavenumber and intensity of the A_{1g}[Nb] phonon mode was successfully applied to probe the phase transition of the SBNN ceramics.

6. Temperature effects on electronic transitions of BFO films

BFO film with the nominal thickness of about 330 nm was prepared on STO (111) substrate by pulsed laser deposition. [5] Fig. 8 shows the XRD pattern of the BFO film and there is no impurity phase. As can be seen, the film is well crystallized with the rhombohedral phase and presents a (111) single crystalline orientation. According to the known Scherrer's equation, the grain size from the (111) diffraction peak was evaluated to about 32 nm. A three-phase layered structure (air/film/substrate) was constructed to

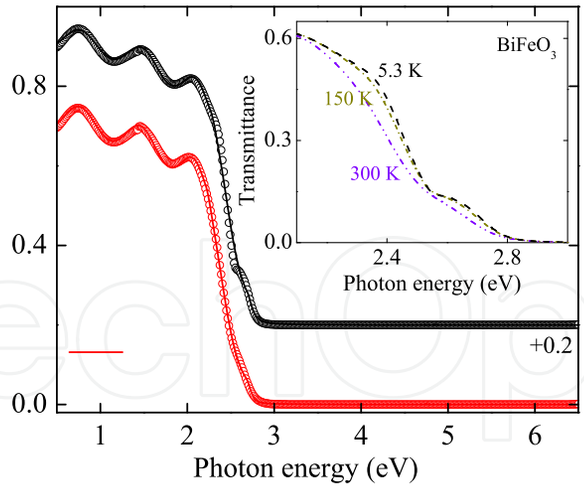

Figure 9. Experimental (dotted curves) and fitting (solid curves) transmittance spectra at temperatures of 300 and 5.3 K, respectively. The inset shows the enlarged band gap region of the BFO film at temperatures of 300, 200, and 5.3 K, respectively. (Figure reproduced with permission from [5]. Copyright 2010, American Institute of Physics.)

simulate the transmittance spectra of the BFO film. It should be emphasized that the normal-incident transmittance spectra cannot be sensitive to the thinner surface rough layer, which could be several nanometers and much less than the film thickness. Therefore, the surface rough layer can be reasonably neglected owing to a slight contribution in the evaluation of the optical properties. The optical constants of the BFO film can be expressed using four Tauc-Lorentz (TL) oscillators. [50] As an example, the experimental and fitting transmittance spectra of the BFO film at 300 and 5.3 K are shown in Fig. 9 with the dotted and solid curves, respectively. Note that the symmetrical interference period indicates that the film is of good uniformity and crystallization. From Fig. 9, it can be observed that the absorption edge remarkably shift toward the lower energy with increasing the temperature, suggesting that the OBG of the film has a negative temperature coefficient. Note that the shift at high temperature region (100-300 K) is larger than that at low temperature region (5.3-100 K). This is because the quantities of the conduction band downward and the valence band upward are different under the distinct temperature regions. Especially, two broadening shoulder structures appear and the intensities become much stronger with decreasing the temperature. The similar phenomena have been observed at 2.5 eV when the temperature decreases to about 4 K, which represents the onset of the optical absorption. [51] Furthermore, the shoulders are simply low-lying features of the electronic structure or evidence for excitonic character.

Based on the theoretical calculations and experimental observations, the four energy bands can be uniquely assigned to the following electronic transitions: (1) on-site Fe^{3+} d to d crystal field transition; (2) majority channel Fe 3d to O 2p charge transfer excitation; (3) minority channel dipole-allowed O p to Fe d charge transfer excitation; and (4) strong hybridized majority channel O p and Fe d to Bi p state excitation, respectively. [51–55] Within the experimental error bars, the energy positions shift toward the higher energy at the temperature of 5.3 K except for the second excitation, which can be attributed to the energy band variations. Nevertheless, the origin of the abnormal shift for the second excitation is unclear in the present work. Under the influence of the tetrahedral crystal field, the Fe 3d orbital states split into t_{2g} and e_g state and the t_{2g} state strongly hybrided with the O p orbital. [52] With decreasing the temperature, the t_{2g} and e_g states can be located at different level in

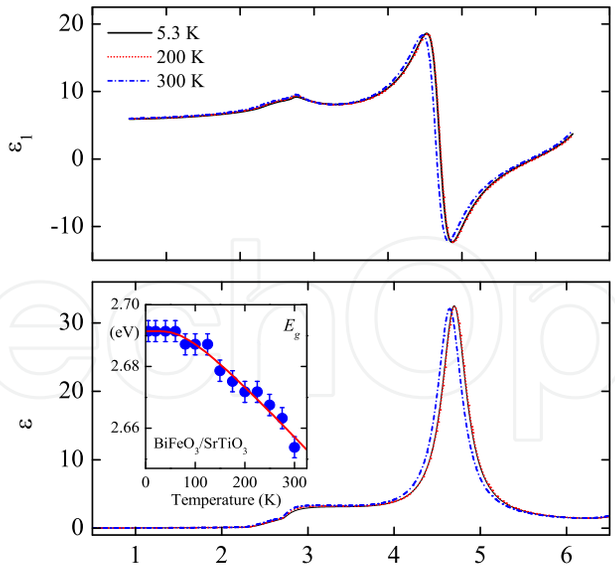

Figure 10. The dielectric functions of the BFO films in the photon energy range of 0.5-6.5 eV at 300, 200, and 5.3 K, respectively. The inset shows the temperature dependence of the E_g (dotted curve) and Bose-Einstein model fitting result (solid curve). (Figure reproduced with permission from [5]. Copyright 2010, American Institute of Physics.)

the energy space, which can affect the electronic excited ability of the Bi, Fe, and O states. On the other hand, the evaluated optical constants of the BFO film is presented in Fig. 10. The real and imaginary parts of dielectric functions increase with the temperature at the lower photon energy while decrease with further increasing the photon energy. With decreasing the temperature, both the ε_1 and ε_2 shift toward the higher energy. The phenomena are related to the modification of the electronic structure such as the fundamental band gap absorption under the lower temperature. From the inset of Fig. 10, it can be found that the E_g value increases from 2.65 ± 0.01 to 2.69 ± 0.01 eV, corresponding to decreasing the temperature from 300 to 5.3 K, which indicates that the total shift value of the E_g is about 40 meV. The observed decrease in the E_g with the temperature can be described using the Bose-Einstein model. It is widely recognized that the electron-phonon interaction and the lattice thermal expansion are responsible for the shrinkage in the optical band gap with the temperature.

7. Conclusion and remarks

In summary, electronic band structures and phase transitions of perovskite (ABO_3)-type Manganese (Mn) doped $Ba_{0.4}Sr_{0.6}TiO_3$ ceramics, $SrBi_{2-x}Nd_xNb_2O_9$, and $BiFeO_3$ materials have been investigated from infrared to ultraviolet transmittance, SE and temperature-dependent Raman scattering techniques. The interband electronic transitions and dielectric functions of these materials could be readily obtained in the wider photon energy region. Meanwhile, the phase transition temperature can be easily determined by phonon scattering measurements, indicating that the present solid state spectroscopy is useful to further clarify the physical phenomena for perovskite-type ferroelectric/multiferroics oxides.

It should be emphasized that optical properties and their related phenomena, such as phase transition and domain status have not been well investigated. The following factors must be addressed: (1) Growth of high-quality perovskite FE materials (crystal, ceramic and

film); (2) Theoretical model and explanations; (3) Improved experimental methods. As for solid state spectroscopic technique, however, it can uniquely discover the electronic band structure of FE system. One can think that the electronic transition will be changed during the phase transition process owing to the crystal structure variation. Thus, we can check the status by recording the spectral response. Evidently, some optical setup at elevated temperatures are necessary because most of FE materials have the high T_C. In our research group, Transmittane/Reflectance, SE, and Raman systems from LHe temperature to about 800 K have been developed. Our next goal is to characterize the physical information of some typical FE materials in a wider spectral and temperature ranges, which play an important role in clarifying the structure transitions and the intrinsic origin.

Acknowledgments

The authors would like to thank Dr. Wenwu Li for valuable discussions. This work was financially supported by the Major State Basic Research Development Program of China (Grant Nos. 2011CB922200 and 2013CB922300), the Natural Science Foundation of China (Grant Nos. 11074076, 60906046 and 61106122), the Program of New Century Excellent Talents, MOE (Grant No. NCET-08-0192) and PCSIRT, the Projects of Science and Technology Commission of Shanghai Municipality (Grant Nos. 11520701300, 10DJ1400201 and 10SG28), and the Program for Professor of Special Appointment (Eastern Scholar) at Shanghai Institutions of Higher Learning.

Author details

Zhigao Hu[1,⋆], Junhao Chu[1,2,⋆],
Yawei Li[1], Kai Jiang[1] and Ziqiang Zhu[1]

1 Key Laboratory of Polar Materials and Devices, Ministry of Education, Department of Electronic Engineering, East China Normal University, Shanghai, People's Republic of China
2 National Laboratory for Infrared Physics, Shanghai Institute of Technical Physics, Chinese Academy of Sciences, Shanghai, People's Republic of China

References

[1] Nagaraj, B.; Sawhney, T.; Perusse, S.; Aggarwal, S.; Ramesh, R.; Kaushik, V. S.; Zafar, S.; Jones, R. E.; Lee, J. -H.; Balu, V. & Lee, J. (1999). (Ba,Sr)TiO_3 thin films with conducting perovskite electrodes for dynamic random access memory applications. *Appl. Phys. Lett.*, 74, 21, 3194-3196

[2] Roy, S. C.; Sharma, G. L. & Bhatnagar, M. C. (2007). Large blue shift in the optical band-gap of sol-gel derived $Ba_{0.5}Sr_{0.5}TiO_3$ thin films. *Solid State Commun.*, 141, 5, 243-247

[3] Kozyrev, A. B.; Kanareykin, A. D.; Nenasheva, E. A.; Osadchy, V. N. & Kosmin, D. M. (2009). Observation of an anomalous correlation between permittivity and tunability of a doped (Ba,Sr)TiO_3 ferroelectric ceramic developed for microwave applications. *Appl. Phys. Lett.*, 95, 01, 012908(1-3)

[4] Catalan, G. & Scott, J. F. (2009). Physics and applications of bismuth ferrite. *Adv. Mater.*, 21, 24, 2463-2485

[5] Li, W. W.; Zhu, J. J.; Wu, J. D.; Gan, J.; Hu, Z. G.; Zhu, M. & Chu, J. H. (2010). Temperature dependence of electronic transitions and optical properties in multiferroic $BiFeO_3$ nanocrystalline film determined from transmittance spectra. *Appl. Phys. Lett.*, 97, 12, 121102(1-3)

[6] Jiang, K.; Zhu, J. J.; Wu, J. D.; Sun, J.; Hu, Z. G. & Chu, J. H. (2011). Influences of oxygen pressure on optical properties and interband electronic transitions in multiferroic bismuth ferrite nanocrystalline films grown by pulsed laser deposition. *ACS Appl. Mater. Interfaces*, 03, 12, 4844-4852

[7] Su, B. & Button, T. W. (2004). Microstructure and dielectric properties of Mg-doped barium strontium titanate ceramics. *J. Appl. Phys.*, 95, 03, 1382-1385

[8] Xu, S.; Qu, Y. & Zhang, C. (2009). Effect of Mg^{2+} content on the dielectric properties of $Ba_{0.65-x}Sr_{0.35}Mg_xTiO_3$ ceramics. *J. Appl. Phys.*, 106, 01, 014107(1-5)

[9] Kim, S. S. & Park, C. (1999). Leakage current behaviors of acceptor- and donor-doped $(Ba_{0.5}Sr_{0.5})TiO_3$ thin films. *Appl. Phys. Lett.*, 75, 17, 2554-2556

[10] Yuan, Z.; Lin, Y.; Weaver, J.; Chen, X.; Chen, C. L.; Subramanyam, G.; Jiang, J. C. & Meletis, E. I. (2005). Large dielectric tunability and microwave properties of Mn-doped $(Ba,Sr)TiO_3$ thin films. *Appl. Phys. Lett.*, 87, 15, 152901(1-3)

[11] Zhang, J. J.; Zhai, J. W. & Yao, X. (2009). Dielectric tunable properties of low-loss $Ba_{0.4}Sr_{0.6}Ti_{1-y}Mn_yO_3$ceramics. *Scripta Mater.*, 61, 07, 764-767

[12] Liu, M.; Ma, C.; Collins, G.; Liu, J.; Chen, C.; Shui, L.; Wang, H.; Dai, C.; Lin, Y.; He, J.; Jiang, J.; Meletis, E. I. & Zhang, Q. (2010). Microwave dielectric properties with optimized Mn-doped $Ba_{0.6}Sr_{0.4}TiO_3$ highly epitaxial thin films. *Cryst. Growth Des.*, 10, 10, 4221-4223

[13] Li, Y. L. & Qu, Y. F. (2009). Dielectric properties and substitution mechanism of samarium-doped $Ba_{0.68}Sr_{0.32}TiO_3$ ceramics. *Mater. Res. Bull.*, 44, 01, 82-85

[14] Zhang, J. J.; Zhai, J. W.; Chou, X. J. & Yao, X. (2008). Influence of rare-earth addition on microstructure and dielectric behavior of $Ba_{0.6}Sr_{0.4}TiO_3$ ceramics. *Mater. Chem. Phys.*, 111, 02, 409-413

[15] Huang, S. M.; Li, Y. C.; Feng, C. D.; Gu, M. & Liu, X. L. (2008). Dielectric and structural properties of layer-structured $Sr_{1-x}Ca_xBi_2Nb_2O_9$. *J. Am. Ceram. Soc.*, 91, 09, 2933-2937

[16] Huang, S. M.; Feng, C. D.; Chen, L. D. & Wen, X. W. (2005). Dielectric properties of $SrBi_{2-x}Pr_xNb_2O_9$ ceramics (x=0, 0.04 and 0.2). *Solid State Commun.*, 133, 6, 375-379

[17] Sun, L.; Feng, C. D.; Chen, L. D. & Huang, S. M. (2007). Effect of substitution of Nd^3 for Bi^3 on the dielectric properties and structures of $SrBi_{2-x}Nd_xNb_2O_9$ bismuth layer-structured ceramics. *J. Appl. Phys.*, 101, 08, 084102(1-5)

[18] Wu, Y.; Forbess, M. J.; Seraji, S.; Limmer, S. J.; Chou, T. P.; Nguyen, C. & Cao, G. (2001). Doping effect in layer structured $SrBi_2Nb_2O_9$ ferroelectrics. *J. Appl. Phys.*, 90, 10, 5296-5302

[19] Liu, G. Z.; Wang, C.; Gu, H. S. & Lu, H. B. (2007). Raman scattering study of La-doped $SrBi_2Nb_2O_9$ ceramics. *J. Phys. D: Appl. Phys.*, 40, 24, 7817-7820

[20] Fang, P.; Fan, H.; Li, J. & Liang, F. (2010). Lanthanum induced larger polarization and dielectric relaxation in Aurivillius phase $SrBi_{2-x}La_xNb_2O_9$ ferroelectric ceramics. *J. Appl. Phys.*, 107, 06, 064104(1-4)

[21] Verma, M.; Sreenivas, K. & Gupta, V. (2009). Influence of La doping on structural and dielectric properties of $SrBi_2Nb_2O_9$ ceramics. *J. Appl. Phys.*, 105, 02, 024511(1-6)

[22] Speghini, A.; Bettinelli, M.; Caldiño, U.; Ramírez, M. O.; Jaque, D.; Bausá, L. E. & Solé, J. G. (2006). Phase transition in $Sr_xBa_{1-x}Nb_2O_6$ ferroelectric crystals probed by Raman spectroscopy. *J. Phys. D: Appl. Phys.*, 39, 23, 4930-4934

[23] Tenne, D. A.; Bruchhausen, A.; Kimura, N. D. L.; Fainstein, A.; Katiyar, R. S.; A. Cantarero,; Soukiassian, A.; Vaithyanathan, V.; Haeni, J. H.; Tian, W.; Schlom, D. G.; Choi, K. J.; Kim, D. M.; Eom, C. B.; Sun, H. P.; Pan, X. Q.; Li, Y. L.; Chen, L. Q.; Jia, Q. X.; Nakhmanson, S. M.; Rabe, K. M. & Xi, X. X. (2006). Probing nanoscale ferroelectricity by ultraviolet Raman spectroscopy. *Science*, 313, 5793, 1614-1616

[24] Zhu, J. J.; Li, W. W.; Xu, G. S.; Jiang, K.; Hu, Z. G. & Chu, J. H. (2011). A phenomenalogical model of electronic band structure in ferroelectric $Pb(In_{1/2}Nb_{1/2})O_3$-$Pb(Mg_{1/3}Nb_{2/3})O_3$-$PbTiO_3$ single crystals around morphotropic phase boundary determined by temperature-dependent transmittance spectra. *Acta Materialia*, 59, 17, 6684-6690

[25] Zhang, W. J.; Li, W. W.; Chen, X. G.; Hu, Z. G.; Liu, W.; Wang, G. S.; Dong, X.L. & Chu, J.H. (2011). Phonon mode and phase transition behaviors of $(1-x)PbSc_{1/2}Ta_{1/2}O_3$-$xPbHfO_3$ relaxor ferroelectric ceramics determined by temperature-dependent Raman spectra. *Appl. Phys. Lett.*, 99, 04, 041902(1-3)

[26] Zhu, J. J.; Li, W. W.; Xu, G.S.; Jiang, K.; Hu, Z. G.; Zhu, M. & Chu, J. H. (2011). Abnormal temperature dependence of interband electronic transitions in relaxor-based ferroelectric $(1-x)Pb(Mg_{1/3}Nb_{2/3})O_3$-$xPbTiO_3$ (x=0.24 and 0.31) single crystals. *Appl. Phys. Lett.*, 98, 09, 091913(1-3)

[27] Chen, X.; Jiang, K.; Hu, Z. G.; Chen, X. F.; Wang, G. S.; Dong, X. L. & Chu, J. H. (2012). Abnormal electronic transition variations of lanthanum-modified lead zironate stannate titanate ceramics near morphotropic phase boundary: A spectroscopic evidence. *Appl. Phys. Lett.*, 101, 01, 011914(1-5)

[28] Liao, Y. Y.; Li, Y. W.; Hu, Z. G. & Chu, J. H. (2012). Temperature dependent phonon Raman scattering of highly *a*-axis oriented $CoFe_2O_4$ inverse spinel ferromagnetic films grown by pulsed laser deposition. *Appl. Phys. Lett.*, 100, 07, 071905(1-4)

[29] Li, W. W.; Yu, Q.; Liang, J. R.; Jiang, K.; Hu, Z. G.; Liu, J.; Chen, H. D.; & Chu, J. H. (2011). Intrinsic evolutions of optical functions, band gap, and higher-energy electronic transitions in VO_2 film near the metal-insulator transition region. *Appl. Phys. Lett.*, 99, 24, 241903(1-3)

[30] Han, M. J.; Jiang, K.; Zhang, J. Z.; Li, Y. W.; Hu, Z. G. & Chu, J. H. (2011). Temperature dependent phonon evolutions and optical properties of highly *c*-axis oriented $CuGaO_2$ semiconductor films grown by the sol-gel method. *Appl. Phys. Lett.*, 99, 13, 131104(1-3)

[31] Yu, W. L.; Jiang, K.; Wu, J. D.; Gan, J.; Zhu, M.; Hu, Z. G. & Chu, J. H. (2011). Electronic structures and excitonic transitions in nanocrystalline iron-doped tin dioxide diluted magnetic semiconductor films: an optical spectroscopic study. *Phys. Chem. Chem. Phys.*, 13, 13, 6211-6222

[32] Wang, J.; Neaton, J. B.; Zheng, H.; Nagarajan, V.; Ogale, S. B.; Liu, B.; Viehland, D.; Vaithyanathan, V.; Schlom, D. G.; Waghmare, U. V.; Spaldin, N. A.; Rabe, K. M.; Wuttig, M. & Ramesh, R. (2003). Epitaxial $BiFeO_3$ multiferroic thin film heterostructures. *Science*, 299, 1719-1722

[33] Singh, M. K. & Katiyar, R. S. (2011). Phonon anomalies near the magnetic phase transitions in $BiFeO_3$ thin films with rhombohedral R_{3C} symmetry. *J. Appl. Phys.*, 109, 07, 07D916(1-3)

[34] Choi, S. G.; Yi, H. T.; Cheong, S. W.; Hilfiker, J. N.; France, R. & Norman, A. G. (2011). Optical anisotropy and charge-transfer transition energies in $BiFeO_3$ from 1.0 to 5.5 eV. *Phys. Rev. B*, 83, 10, 100101(R)(1-4)

[35] Basu, S. R.; Martin, L. W.; Chu, Y. H.; Gajek, M.; Ramesh, R.; Rai, R. C.; Xu, X. & Musfeldt, J. L. (2008). Influence of sample processing parameters on thermal boundary conductance value in an Al/AlN system. *Appl. Phys. Lett.* 92, 09, 091905(1-3)

[36] Balke, N.; Choudhury, S.; Jesse, S.; Huijben, M.; Chu, Y. H.; Baddorf, A. P.; Chen, L. Q.; Ramesh, R. & Kalinin, S. V. (2009). Deterministic control of ferroelastic switching in multiferroic materials. *Nature Nanotechnology*, 4, 12, 868-875

[37] Yang, S. Y.; Martin, L. W.; Byrnes, S. J.; Conry, T. E.; Basu, S. R.; Paran, D.; Reichertz, L.; Ihlefeld, J.; Adamo, C.; Melville, A.; Chu, Y. H.; Yang, C. H.; Musfeldt, J. L.; Schlom, D. G.; Ager, I. J. W. & Ramesh, R. (2009). Photovoltaic effects in $BiFeO_3$. *Appl. Phys. Lett.*, 95, 06, 062909(1-3)

[38] Choi, T.; Lee, S.; Choi, Y. J.; Kiryukhin, V. & Cheong, S.-W. (2009). Switchable ferroelectric diode and photovoltaic effect in $BiFeO_3$. *Science*, 324, 5923, 63-66.

[39] Jiang, K.; Zhang, J. Z.; Yu, W. L.; Hu, Z. G. & Chu, J. H. (2012). Manganese doping effects on interband electronic transitions, lattice vibrations, and dielectric functions of perovskite-type $Ba_{0.4}Sr_{0.6}TiO_3$ ferroelectric ceramics. *Appl. Phys. A-Mater. Sci. Process.*, 106, 04, 877-884

[40] Zhu, M.; Sun, L.; Li, W. W.; Yu, W. L.; Li, Y. W.; Hu, Z. G. & Chu, J. H. (2010). Lattice vibrations and dielectric functions of ferroelectric $SrBi_{2-x}$,$Nd_xNb_2O_9$ bismuth

layer-structured ceramics determined by infrared reflectance spectra. *Mater. Res. Bull.*, 45, 11, 1654-1658

[41] Yu, W. L.; Li, W. W.; Wu, J. D.; Sun, J.; Zhu, J. J.; Zhu, M.; Hu, Z. G. & Chu, J. H. (2010). Far-infrared-ultraviolet dielectric function, lattice vibration, and photoluminescence properties of diluted magnetic semiconductor $Sn_{1-x}Mn_xO_2/c$-sapphire nanocrystalline films. *J. Phys. Chem. C*, 114 , 18, 8593-8600

[42] Kohiki, S.; Arai, M.; Yoshikawa, H.; Fukushima, S.; Oku, M. & Waseda, Y. (2000). Energy-loss structure in core-level photoemission satellites of $SrTiO_3$, $SrTiO_3$:La, and $SrTiO_3$:Nb. *Phys. Rev. B*, 62, 12, 7964-7969

[43] Warren, W. L.; Vanheusden, K.; Dimos, D.; Pike, G. E. & Tuttle, B. A. (1996). Oxygen vacancy motion in perovskite oxides. *J. Am. Ceram. Soc.*, 79, 02, 536-538

[44] Burstein, E. (1954). Anomalous optical absorption limit in InSb. *Phys. Rev.*, 93, 03, 632-633

[45] Graves, P. R.; Hua, G.; Myhra, S. & Thompson, J. G. (1995). The Raman modes of the Aurivillius phases: Temperature and polarization dependence. *J. Solid State Chem.*, 114, 01, 112-122

[46] Jiang, K.; Chen, X. G.; Li, W. W.; Zhan, Z. N.; Sun, L.; Hu, Z. G. & Chu, J. H. (2012). Doping effect on the phase transition temperature in ferroelectric $SrBi_{2-x}Nd_xNb_2O_9$ layer-structured ceramics: A micro-Raman scattering study. *J. Raman Spectrosc.*, 43, 04, 583-587

[47] Liang, K.; Qi, Y. J. & Lu, C. J. (2009). Temperature-dependent Raman scattering in ferroelectric $Bi_{4-x}Nd_xTi_3O_{12}$ (x=0, 0.5, 0.85) single crystals. *J. Raman Spectrosc.*, 40, 12, 2088-2091

[48] Dobal, P. S. & Katiyar, R. S. (2002). Studies on ferroelectric perovskites and Bi-layered compounds using micro-Raman spectroscopy. *J. Raman Spectrosc.*, 33, 06, 405-423

[49] Kitaev, Y. E.; Aroyo, M. I. & Mato, J. M. P. (2007). Site symmetry approach to phase transitions in perovskite-related ferroelectric compounds. *Phys. Rev. B*, 75, 06, 064110(1-11)

[50] Jellison, G. E. Jr. & Modine, F. A. (1996). Parameterization of the optical functions of amorphous materials in the interband region. *Appl. Phys. Lett.*, 69, 03, 371-373. Erratum: "Parameterization of the optical functions of amorphous materials in the interband region". 69, 03, 2137

[51] Basu, S. R.; Martin, L. W.; Chu, Y. H.; Gajek, M.; Ramesh, R.; Rai, R. C.; Xu, X. & Musfeldt, J. L. (2008). Photoconductivity in $BiFeO_3$ thin films. *Appl. Phys. Lett.*, 92, 09, 091905(1-3)

[52] Chen, P.; Podraza, N. J.; Xu, X. S.; Melville, A.; Vlahos, E.; Gopalan, V.; Ramesh, R.; Schlom, D. G. & Musfeldt, J. L. (2010). Optical properties of quasi-tetragonal $BiFeO_3$ thin films. *Appl. Phys. Lett.*, 96, 13, 131907(1-3)

[53] Xu, X. S.; Brinzari, T. V.; Lee, S.; Chu, Y. H.; Martin, L. W.; Kumar, A.; McGill, S.; Rai, R. C.; Ramesh, R.; Gopalan, V.; Cheong, S. W. & Musfeldt, J. L. (2009). Optical properties and magnetochromism in multiferroic $BiFeO_3$. *Phys. Rev. B*, 79, 13, 134425(1-4)

[54] Ramirez, M. O.; Kumar, A.; Denev, S. A.; Podraza, N. J.; Xu, X. S.; Rai, R. C.; Chu, Y. H.; Seidel, J.; Martin, L. W.; Yang, S. -Y.; Saiz, E.; Ihlefeld, J. F.; Lee, S.; Klug, J.; Cheong, S. W.; Bedzyk, M. J.; Auciello, O.; Schlom, D. G.; Ramesh, R.; Orenstein, J.; Musfeldt, J. L. & Gopalan, V. (2009). Magnon sidebands and spin-charge coupling in bismuth ferrite probed by nonlinear optical spectroscopy. *Phys. Rev. B*, 79, 22, 224106(1-9)

[55] Ramirez, M. O.; Kumar, A.; Denev, S. A.; Chu, Y. H.; Seidel, J.; Martin, L. W.; Yang, S. -Y.; Rai, R. C.; Xue, X. S.; Ihlefeld, J. F.; Podraza, N. J.; Saiz, E.; Lee, S.; Klug, J.; Cheong, S. W.; Bedzyk, M. J.; Auciello, O.; Schlom, D. G.; Orenstein, J.; Ramesh, R.; Musfeldt, J. L.; Litvinchuk, A. P. & Gopalan, V. (2009). Spin-charge-lattice coupling through resonant multimagnon excitations in multiferroic $BiFeO_3$. *Appl. Phys. Lett.*, 94, 16, 161905(1-3)

IntechOpen